CO2 and H2 Adsorption and Reaction at Nin/YSZ(111) Interfaces: A Density Functional Theory Study

Abdelaziz Cadi-Essadek,[†] Alberto Roldan,[†] Xavier Aparicio-Anglès,[‡] and Nora H. de Leeuw*,[†,‡]

[†]School of Chemistry, Cardiff University, Main Building, Park Place, CF10 3AT Cardiff, U.K.

[‡]Department of Chemistry, University College London, 20 Gordon Street, London WC1H 0AJ, U.K.

ABSTRACT: To recycle CO_2 into sustainable fuels and chemicals, coelectrolysis of CO_2 and H_2O can be achieved in solid oxide electrolysis cells, where the molecules are supplied to the Ni/YSZ electrode (YSZ = yttria-stabilized zirconia). Oxygen diffusion along the electrode has been identified as the critical step in the process, where YSZ is the common catalyst support. We have investigated the interaction of a CO_2 molecule with the clean YSZ(111) surface and with Ni_n/YSZ(111) (n = 1, 4−7, 10, and 20) interfaces, using a spin-polarized density functional theory and a long-range dispersion correction. Here, we have considered up to six initial adsorption sites and two orientations for the CO_2 molecule, which showed that the adsorption is stronger at the Ni_n/YSZ(111) (n = 4−7, 10, and 20) interface than on the clean YSZ(111) and Ni_1/YSZ(111) systems. Additionally, we have determined that the preferential adsorption site of CO_2 is at the interface between the Ni clusters and the YSZ(111) surface. We have observed a bending and stretching of the molecule, demonstrating its activation upon adsorption, because of charge transfer between the metal cluster and the molecule and a mixing between Ni orbitals and CO_2 orbitals. In this work, we show that although the electronic structure of the clusters depends on the cluster size, the interaction strength of CO_2 with the interface is independent of the size of the supported nickel particle. Finally, we have considered the reverse water gas shift reaction and determined the hydrocarboxylic intermediate in the reaction mechanism over Ni_5/YSZ(111).
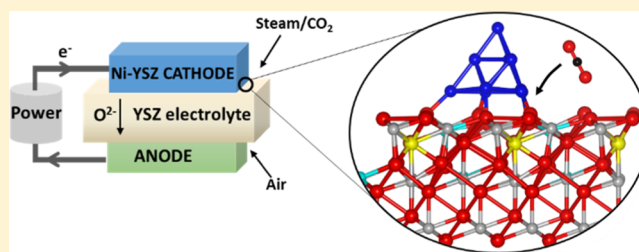
1. INTRODUCTION

Significant efforts have been dedicated to the identification of a catalytic system, which is capable of sustainably converting CO_2 to liquid fuels and chemicals, where the activation of CO_2 is a key step in the conversion process.[1] For instance, coelectrolysis of CO_2 and H_2O could be used in solid oxide fuel cells (SOFCs) to recycle CO_2 into sustainable hydrocarbon fuels.[2−9] During the cell operation, both CO_2 and H_2O are supplied to the anode of the fuel cell,[4] where they interact with the catalyst.

SOFCs have three main components: two porous electrodes separated by an oxygen ion-conducting electrolyte. As the working temperature of the SOFC is high, from 773 to 1173 K, these devices present several advantages, including efficiency, reliability, modularity, fuel flexibility, and low pollutant emission.[10−21] Ni/YSZ (YSZ = yttria-stabilized zirconia) is an appropriate anode for the SOFC, as this system is stable at high temperatures, is electronically conducting, and has porosity to maximize the contact area with the fuel.[11] Ni/YSZ is a cermet, which is a ceramic matrix, here YSZ, containing supported metal (Ni) nanoparticles. The Ni nanoparticles and YSZ provide electronic and oxygen-ion conductivities, respectively.[4,22−25]

YSZ is obtained from doping cubic zirconia (c-ZrO_2) with yttria (Y_2O_3). At atmospheric pressure, pure zirconia (ZrO_2) has three polymorphs: below 1400 K, the stable phase is monoclinic; between 1400 and 2650 K, ZrO_2 is tetragonal; and between 2650 and 2950 K (polymorph melting point), cubic ZrO_2 (c-ZrO_2) is the most stable structure.[26,27] However, c-ZrO_2 is the stable phase at a lower temperature (below 800 K) when it is doped with Y_2O_3 to form YSZ, which increases the ionic conductivity of the material and is therefore the phase employed in SOFCs.

In the SOFC, the key reactions occur at the triple phase boundary (TPB) where the anode, the electrolyte, and the fuel meet,[28−30] hence our interest in the interaction of Ni/YSZ with gas molecules such as CO_2, CO, H_2O, and H_2. H_2/CO mixtures can be used as a fuel in the SOFC, and therefore, reactions such as the water-gas shift reaction (WGSR) can take place.[31−33] Following other authors, who have used density functional theory (DFT) calculations to study the interaction of CO_2 with metal−oxide interfaces,[34,35] we have used a similar methodology to focus on the interaction of CO_2 with different cluster sizes of the nickel particle supported on YSZ.

Studies of the adsorption and activation of CO_2 on other metal−oxide systems,[36,37] such as M_2/γ-Al_2O_3 (M = Sc−Cu), have shown a charge transfer from the oxide-supported metal to the CO_2 molecule, leading to the adsorption and bending of

CO_2.[1] Pan et al.[38] have studied CO_2 hydrogenation on Ni/γ-Al_2O_3, where they adsorbed separately CO_2 and H adatoms on supported Ni_4 clusters before describing the coadsorption of both molecules. On the clean Ni_4/γ-Al_2O_3, they found that CO_2 interacts with two Ni atoms via its C atom and both O atoms, where the molecule is activated as shown by the bending and elongation of C−O bonds upon adsorption. They have also explored the elementary steps in CO_2 conversion, typically to formate and carboxyl groups, on both dry and hydrogenated Ni/γ-Al_2O_3 surfaces. Here, they showed that on the clean surface, the formation of formate is kinetically feasible, whereas the pathway leading to CO is thermodynamically more favorable. However, on the hydroxylated surface, CO formation is preferred both kinetically and thermodynamically.

Another CO_2 hydrogenation study on Cu/ZnO($000\overline{1}$)[39] has confirmed the importance of the supported metal cluster in the reaction mechanism: the authors showed at a theoretical level that the reaction is faster on the supported Cu clusters than on the Cu(111) surface, owing to low-coordinated Cu sites that contribute to the stabilization of the reaction intermediates. Similarly, Vidal et al.[40] showed that CO_2 activation is more favorable on Cu/TiC than on the Cu(111) surface. The adsorption of CO_2 over Cu−Co supported on γ-Al_2O_3 showed CO_2 activation upon adsorption, where the hydroxylated surface stabilized the adsorbed CO_2 by either hydrogen bonding or protonating CO_2.[41] Tang et al.[42] used first principles kinetic Monte Carlo simulations to study the hydrogenation of CO_2 on the Cu/ZrO_2 interface. In their investigation, the authors described the interaction of CO_2 with Cu/ZrO_2, where they showed that CO_2 prefers to adsorb on the naked ZrO_2 surface, rather than at the Cu/ZrO_2 interface. They calculated an adsorption energy of 0.69 eV and also described the bending of the molecule upon adsorption. They also noted a stretching of the C−O bonds and charge transfer from the ZrO_2 surface to the antibonding $2\pi_u$ orbital of CO_2.

Despite these studies, a systematic investigation of the effect of the size of the supported metal clusters on CO_2 adsorption and potential activation is still lacking. Here, we have studied the interaction of eight systems [YSZ(111) and Ni_n/YSZ(111) (n = 1, 4−7, 10, and 20)] with a CO_2 molecule, and we have analyzed the geometric structure and vibrational frequencies to describe the configuration of the adsorbed molecule at the interface. We have also characterized the electronic structure to evaluate the charge transfer between the interfacial systems and the CO_2 molecule. Finally, we have investigated the reverse WGSR mechanism, which is the reaction between the adsorbed CO_2 molecule and H_2 to generate water and carbon monoxide.

2. COMPUTATIONAL METHODS AND MODELS

Cubic zirconia (c-ZrO_2) has the fluorite structure and therefore a face-centered cubic (fcc) unit cell (space group $Fm3m$). The Zr atoms constitute the fcc cube, and each Zr atom is coordinated to eight oxygen atoms which are located on the diagonals of the cube. To model the most stable cubic zirconia surface, the ZrO_2(111) O-terminated surface,[43,44] we have cleaved the c-ZrO_2 bulk using the METADISE code[45] and created a slab model, similarly to our previous investigation.[44] The ZrO_2(111) slab contains nine atomic layers (three O−Zr−O trilayers), where the five top atomic layers were relaxed during geometry optimization and the four

layers in the bottom were kept fixed to represent the bulk crystal. The YSZ(111) surface was built by the substitution of two Zr layers (from the top and the sub O−Zr−O trilayers) by two Y atoms (9.1 w % of yttria) with the consequent removal of one oxygen atom from the third atomic layer (the next-nearest neighbor of Y atoms). The side and top views of ZrO_2(111) and YSZ(111), respectively, are shown in Figure 1.
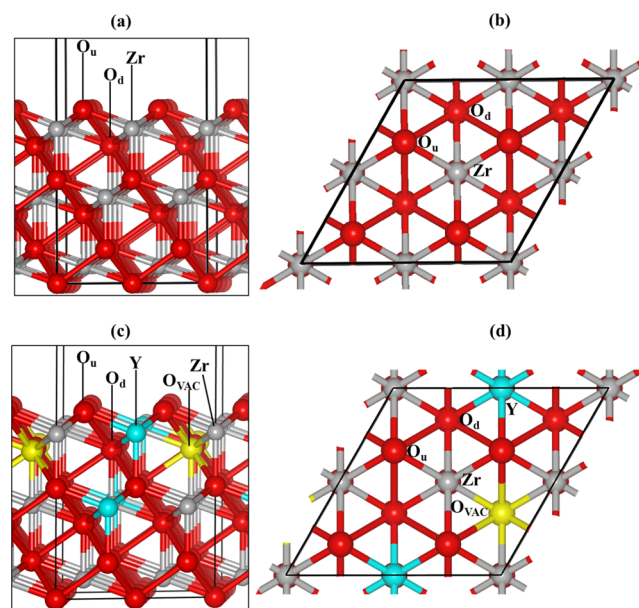

Figure 1. (a,b) Side and top views, respectively, of the oxygen-terminated ZrO_2(111) surface. (c,d) Side and top views, respectively, of the YSZ(111) surface. Color key: O, Zr, and Y are represented by red, gray, and cyan spheres, respectively. The yellow spheres represent the oxygen vacancy.

The location of the Y dopants and oxygen vacancy were determined in previous works.[44,46,47] We have described all the nonequivalent positions of the Y atoms and oxygen vacancy, and here, we show the most stable structure (Figure 1c,d). The unit formula represented in Figure 1c,d is $Zr_{10}Y_2O_{23}$. In this structure, the Y atoms are located in the top and sub O−Zr−O trilayers, whereas the oxygen vacancy is positioned in the lower oxygen layer of the top O−Zr−O trilayers.

We have repeated the unit cell in the x and y surface directions to avoid lateral interactions between the Ni_n clusters; thus, our YSZ(111) surface is modeled by a $Zr_{40}Y_8O_{92}$(111) slab. We first tried several nonequivalent geometries and initial adsorption sites for the Ni_n clusters,[48] which showed that the most stable configuration for the clusters is a pyramid shape, rather than a flat shape on top of the YSZ(111) surface, indicating that the binding between the Ni atoms is stronger than the interaction to the surface. Tosoni et al.[49] have adsorbed Ni_{10} clusters on top of a similar surface, i.e., tetragonal ZrO_2(101), and they also showed that the metal clusters prefer to adopt a three-dimensional shape rather than a flat configuration.

In addition, we observed that the Ni_n clusters adsorb away from the Y atoms. Figure 2 shows the most stable Ni_n/YSZ(111) (n = 1, 4−7, 10, and 20) configurations, which we have considered for the adsorption of the CO_2 molecule, where the average size of the Ni_n clusters ranges from 3.63 Å^2 (n = 4) to 41.10 Å^2 (n = 20).
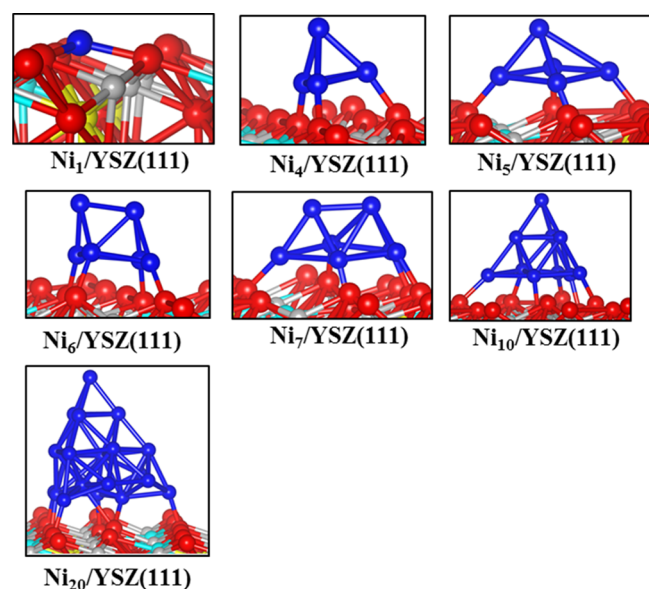
Figure 2. Stable configurations of Ni$_n$ (n = 1, 4–7, 10, and 20) clusters adsorbed on the YSZ(111) surface. Color key: O, Zr, Y, and Ni are represented by red, gray, cyan, and blue spheres, respectively. The yellow spheres represent the oxygen vacancy.

The calculations in this study are based on spin-polarized DFT and performed by solving the Kohn–Sham equations[50] in a periodic system, as implemented in the Vienna Ab-initio Simulation Package.[51–54] Exchange–correlation potentials are modeled by the general gradient approximation[55] using the Perdew–Burke–Ernzerhof density functional. The long-range dispersion interactions were described by the semiempirical method of Grimme,[56] which showed an improvement in the description of the molecular adsorption.[57–59] The C (2s, 2p), O (2s, 2p), Ni (3d, 4s), Zr (4d, 5s), and Y (4s, 4p, 4d, 5s) electrons have been treated explicitly as valence states, whereas the inner electrons were considered as core electrons and kept frozen. The core–valence electron interaction has been treated with the projected augmented wave method.[60] A plane-wave kinetic energy cutoff of 500 eV has proven to accurately describe the geometry and electronic structure.[61–63] Geometry optimization has been performed using the conjugate gradient technique with an interatomic force threshold of 0.01 eV/Å. Monkhorst–Pack grids of 3 × 3 × 1 k-point sampling were used for the 2 × 2 slab calculations. In our previous study,[44] we

calculated the band gap of ZrO$_2$(111) to be 3.14 eV, which, as expected from the DFT calculations, is lower than the experimental bulk values (~5–6 eV),[64,65] but in good agreement with previous computational investigations.[62,66] The gas-phase CO$_2$ molecule was placed in a large box (14 × 15 × 16 Å^3) in order to avoid lateral interactions using 1 × 1 × 1 k-point sampling.

The vibrational frequencies of CO$_2$ (in the gas phase and adsorbed on the surface) were calculated by finite displacements of every coordinate, where the eigenvectors of the Hessian matrix correspond to the vibrational normal modes. The CO$_2$ frequency changes, upon adsorption, reflect an alteration of interatomic bonds. For example, a shift toward higher frequency values indicates stronger bonds. To evaluate the atomic charges in the system, we employed Bader analysis as implemented in the Henkelman algorithm.[67]

3. RESULTS AND DISCUSSION

3.1. Geometry. We have first evaluated the interaction of CO$_2$ with both the bare YSZ(111) and the Ni$_n$/YSZ(111) surfaces and have calculated the binding energy (E_B) of CO$_2$ on the surfaces as follows (eq 1)

$$E_B = E_{CO_2-surface} - (E_{surface} + E_{CO_2}) \qquad (1)$$

where $E_{CO_2-surface}$ is the energy of the YSZ(111) surface (with or without the Ni$_n$ cluster) and the adsorbed CO$_2$ and $E_{surface}$ and E_{CO_2} are the energies of the surface system without CO$_2$ and the CO$_2$ molecule in the gas phase, respectively. A positive binding energy reflects an endothermic CO$_2$ adsorption, whereas a negative binding energy reflects an exothermic CO$_2$ adsorption and therefore a favorable interaction between CO$_2$ and the Ni$_n$/YSZ(111) interface.

We have tried several initial adsorption sites for CO$_2$ on the clean YSZ(111) surface and on the supported Ni$_n$ clusters on YSZ(111). On Ni$_n$/YSZ(111), CO$_2$ has been initially adsorbed on the top and edge of the Ni$_n$ cluster, at the interface between the Ni$_n$ cluster and the oxide surface, and away from the Ni$_n$ cluster. We have considered at least two CO$_2$ orientations for each initial adsorption site, and Figure 3 shows the energetically most favorable adsorption geometries. We have also investigated the adsorption of CO$_2$-derived carbonates on the clean YSZ(111) surface, where the CO$_2$ molecule is activated, and the carbon and oxygen interact with the surface oxygen and metal (Zr and Y) atoms, respectively (Figure 3).
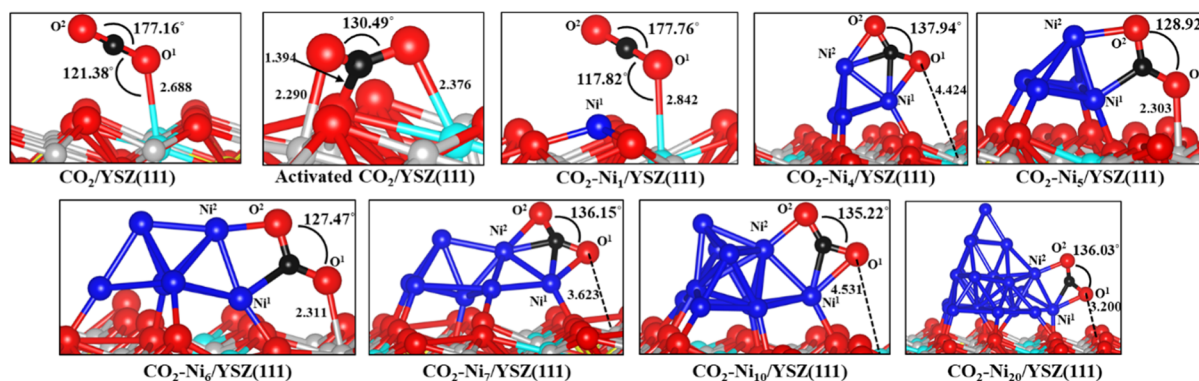

Figure 3. Most stable configurations of CO$_2$/YSZ(111) and CO$_2$–Ni$_n$/YSZ(111). Color key: O, Zr, Y, Ni, and C are represented by red, gray, cyan, blue, and black spheres, respectively. The yellow spheres represent the oxygen vacancy. All distances are in angstrom.

Table 1. Calculated Binding Energy (E_B, in eV), Distances (in Å), O−C−O Angle (θ_{OCO}, in Degrees), and Charge (q, in e$^-$) of CO_2 Adsorbed on the YSZ(111) and Ni_n/YSZ(111) (n = 1, 4−7, 10, and 20) interfaces

surface	E_B	CO internal bonds		CO_2-surf atom distance	CO_2–Ni_n distance				θ_{OCO}	total charge before CO_2 adsorption	total charge upon CO_2 adsorption	
		C–O^1	C–O^2		C–Ni^1	C–Ni^2	O^1–Ni^1	O^2–Ni^2		q_{Ni_n}	q_{Ni_n}	q_{CO_2}
YSZ(111)	−0.37	1.183	1.170	2.688					177.16			0.0
Ni$_1$/YSZ(111)	−0.32	1.181	1.172	2.842	3.655		4.555		177.76	+0.3	+0.3	0.0
Ni$_4$/YSZ(111)	−1.16	1.253	1.256	4.424	1.971	1.981	2.075	2.065	137.94	+0.1	+0.7	−0.7
Ni$_5$/YSZ(111)	−1.20	1.265	1.274	2.303	1.884	2.430	2.706	2.019	128.92	+0.2	+0.8	−0.8
Ni$_6$/YSZ(111)	−1.66	1.260	1.288	2.311	1.859	2.451	2.757	1.895	127.47	+0.2	+0.8	−0.8
Ni$_7$/YSZ(111)	−1.24	1.263	1.260	3.623	1.939	1.984	2.083	2.051	136.15	+0.2	+0.8	−0.8
Ni$_{10}$/YSZ(111)	−1.20	1.247	1.268	4.531	1.899	2.141	2.230	1.971	135.22	+0.2	+0.9	−0.7
Ni$_{20}$/YSZ(111)	−1.49	1.265	1.256	3.200	1.888	2.108	2.091	2.029	136.03	+0.2	+1.0	−0.7

On the clean surface, the linear CO_2 prefers to adsorb near the Y atom with a binding energy of −0.37 eV (Table 1) and adopting a tilted position. The activated CO_2 adsorbs with a binding energy of −0.49 eV. However, we will not discuss any further about the different activated CO_2 isomers on the clean surface, as we are primarily interested in CO_2 adsorption at the Ni/YSZ interface, which is our model for the TPB in SOFCs. Upon adsorption, CO_2 remains linear with an angle between the molecule and the surface of 121.38°. The CO_2−surface distance is 2.688 Å, and the average internal C−O bond is 1.177 Å, which is similar to the C−O distance calculated for the gas-phase molecule, indicating that the CO_2−surface interaction is weak and the molecule remains nonactivated. This CO_2−YSZ(111) interaction has been discussed in detail in our previous work.[68] Chen et al.[69] found a weaker adsorption for linear CO_2 on top of the (111) surface of pure tetragonal ZrO_2 (−0.05 eV) because of the non-consideration of the dispersion forces.

In Figure 3, we observe that CO_2−YSZ(111) and CO_2−Ni$_1$/YSZ(111) have a similar geometry and comparable binding energies: −0.37 and −0.32 eV, respectively (Table 1). On Ni$_1$/YSZ(111), CO_2 adsorbs at a distance of 2.842 Å from the yttrium atom and the average internal C−O bond is 1.177 Å; the molecule also remains linear and forms an angle of 117.82° with the oxide surface. Thus, one Ni atom does not affect significantly the CO_2 adsorption properties of the YSZ(111) surface.

From Table 1, we note that for Ni$_n$ ($n \geq 4$) clusters supported on the YSZ(111) interface, E_B is −1.16 eV or larger, which is approximately 3 times stronger than the binding energies found on either CO_2/YSZ(111) or CO_2−Ni$_1$/YSZ(111), indicating that the Ni$_n$ ($n \geq 4$) clusters stabilize CO_2 adsorption. Our calculated binding energies for CO_2−Ni$_n$/YSZ(111) ($n \geq 4$) are in the same range as the one obtained by Pan et al.[38] (0.93 eV) in their study of CO_2 hydrogenation on Ni/γ-Al$_2$O$_3$. From Figure 3, we note that CO_2 adsorbs on the edge of the cluster, at the interface with the YSZ(111), where the C atom binds at least one Ni atom: the C−Ni distance ranges from 1.859 to 2.451 Å for the Ni$_n$/YSZ(111) (n = 4−7, 10, and 20) interfaces (Table 1). These calculated C−Ni distances at the Ni$_n$/YSZ(111) (n = 4−7, 10, and 20) interfaces are comparable to the study by Hahn et al.,[35] where they found a C−Ni distance of 1.89 Å and showed that CO_2 adsorbs on top of the Ni$_{10}$/CeO$_2$(111) surface with similar geometries to the ones presented in Figure 3.

We find that CO_2 further interacts with Ni$_n$ clusters through its oxygen atoms (O^1 and O^2) at distances ranging from 1.8 to

1.9 Å (Table 1). The YSZ(111) surface also plays a role in the CO_2 adsorption because the CO_2 oxygen atom that points toward the surface interacts with Zr atoms, as shown in Figure 3. The O^1−surface distance varies depending on the cluster shape: for the geometries where the cluster is slightly tilted toward the surface, i.e., CO_2−Ni$_5$/YSZ(111) and CO_2−Ni$_6$/YSZ(111), the O^1−surface distance is shorter than the one found in the geometries where the cluster adopts a configuration parallel to the surface, i.e., CO_2−Ni$_n$/YSZ(111) (n = 4, 7, 10, and 20) (Table 1 and Figure 3).

In Figure 4 we have plotted the average of the difference between the internal C−O^1 and C−O^2 distances in the gas
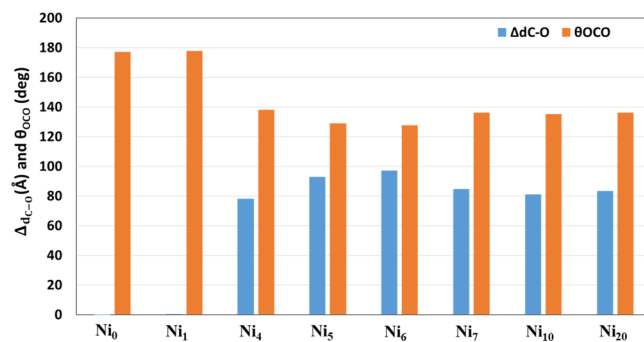
Figure 4. Elongation ($\Delta_{d_{C-O}}$, in Å) and angle (θ_{OCO}, in deg) of CO_2 adsorbed on the YSZ(111) and Ni$_n$/YSZ(111) (n = 1, 4−7, 10, and 20) interfaces. Note that we have multiplied by 10^3 the elongation $\Delta_{d_{C-O}}$ to facilitate the reading of the graph.

phase and after adsorption of CO_2 on the YSZ(111) and Ni$_n$/YSZ(111) (n = 1, 4−7, 10, and 20) interfaces from $\Delta_{d_{C-O}} = \frac{(d_{C-O^1} - 1.177) + (d_{C-O^2} - 1.177)}{2}$, where 1.177 Å is the internal C−O distance in the gas phase. We have also plotted the molecule's angle for the latter configurations, and the calculated values of C−O^1, C−O^2, and θ_{OCO} are shown in Table 1.

Figure 4 clearly shows that the internal C−O bonds vary only weakly upon CO_2 adsorption on both the YSZ(111) (Ni$_0$) and the N$_1$/YSZ(111) interfaces. However, on the Ni$_n$/YSZ(111) (n = 4−7, 10, and 20) interface where CO_2 chemisorbs, the internal C−O elongation is more notable: $\Delta_{d_{C-O}}$ ranges from 0.078 to 0.097 Å. Additionally, we note that the stretching of the C−O internal bonds is asymmetric as shown in Table 1: generally, the C−O^2 distance (involving the
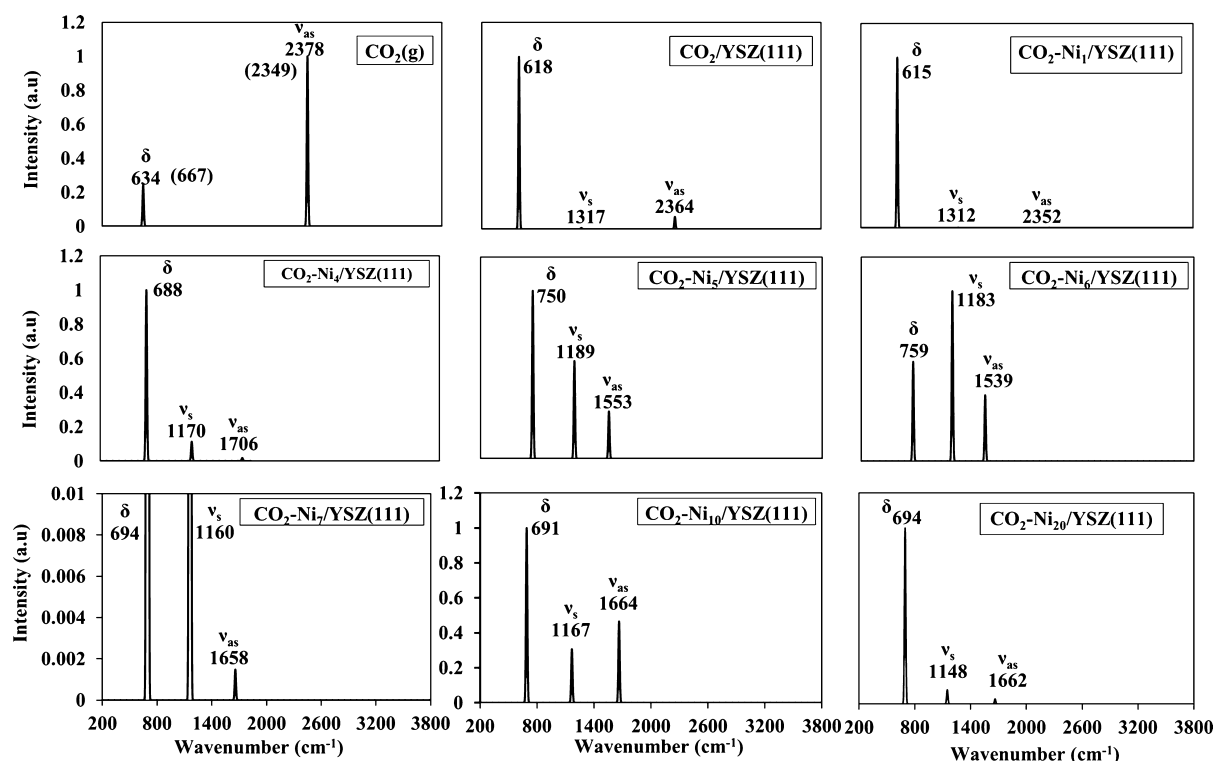
Figure 5. Modeled IR spectra of CO_2 in the gas phase and on the naked YSZ(111) and on the CO_2–Ni_n/YSZ(111) (n = 1, 4–7, 10, and 20) interfaces. The insets in parenthesis are the IR experimental values from the literature.[70]

oxygen pointing toward the gas phase) is larger than the C–O^1 distance, except on the Ni_7/YSZ(111) and Ni_{20}/YSZ(111) interfaces. This asymmetric stretching upon CO_2 adsorption on the Ni_n/YSZ(111) interfaces suggests that O^2 would dissociate more easily than O^1 from the molecule, as was also suggested by Hahn et al.[35] This asymmetry provides insights into the mechanism of the CO_2 reduction in SOFCs: the hydrogenation of O^2 may lead to CO + H_2O, yielding CH_3OH, whereas HCOOH may be the product of the hydrogenation of O^1.

The CO_2 activation is confirmed by the O–C–O angle analysis (Figure 4). CO_2 bending is more pronounced upon adsorption on supported clusters than on the clean YSZ(111) surface or on a single Ni atom catalyst. As expected, for the strongest adsorption, we obtained the smallest angle (CO_2–Ni_6/YSZ(111)) and most pronounced bending. This CO_2 activation has also been observed on similar systems,[1] where the authors showed that CO_2 prefers to adopt a bent geometry on top of its most favorable adsorption site: the interface between the oxide support ($γ$-Al_2O_3) and the transition metal dimer (Sc–Cu).

3.2. Frequency Analysis. In Figure 5 we have plotted the infrared (IR) spectra of CO_2 adsorbed on pristine and Ni_n-decorated YSZ(111) surfaces and compared them with the IR spectra of CO_2 in the gas phase. The variation in the peak position upon the adsorption of the molecule confirms the change in the CO_2 geometry and weakening of the intramolecular bonds. We have also compared the IR spectra of the adsorbed molecule with the experimental data to characterize the structures determined in this work and validate the geometries of the CO_2 adsorbed on the Ni_n/YSZ(111) interfaces.

In the gas phase, CO_2 has two calculated vibrational modes active in IR: the asymmetrical stretching ($ν_{as}$ = 2378 cm^{-1}) and

the bending ($δ$ = 634 cm^{-1}) modes. As shown in Figure 5, our calculated values of CO_2 IR in the gas phase are in good agreement with the experimental values from the literature (667 and 2349 cm^{-1} for $δ$ and $ν_{as}$, respectively).[70]

Upon adsorption on YSZ(111) and Ni_1/YSZ(111), the average shift of the asymmetrical stretching is 20 cm^{-1}, which is in good agreement with the weak adsorption energy and small internal bond elongation of CO_2 upon adsorption. Our calculated IR values for CO_2 on YSZ(111) are in good agreement with the experimental study made by Ramis et al., who studied the weak adsorption of CO_2 species on ZrO_2 (2362 and 1378 cm^{-1} for $ν_{as}$ and $ν_{ss}$, respectively).[71]

On the Ni_n/YSZ(111) (n = 4–7, 10, 20) interfaces, where CO_2 adsorbs strongly, we note an average shift of 748 cm^{-1} of the asymmetrical stretching mode. The reason for this decrease is the weakening of the CO_2 internal bond upon adsorption. This shift confirms the geometrical analysis, where we showed an increase of the C–O distances and an increase of the $θ_{OCO}$ bending. Mudiyanselage et al.[72] have studied WGSR on a similar system, i.e., the CeO_x/Cu(111) interface. They showed experimentally and theoretically by DFT a 700 cm^{-1} shift in $ν_{as}$ upon CO_2 adsorption at the interface, which is in the same range as our value (748 cm^{-1}). Graciani et al.[73] have also shown experimentally that the CeO_x/Cu(111) interface activates CO_2, as they observed two IR peaks at 1288 and 1610 cm^{-1} corresponding to the presence of a carboxylate species ($CO_2^{δ-}$) on the surface.[74] These values agree with our findings on the Ni_n/YSZ(111) (n = 4–7, 10, 20) interfaces, where $ν_s$ and $ν_{as}$ are at 1170 and 1630 cm^{-1}, respectively.

Figure 5 also indicates that the symmetrical stretching ($ν_s$) of adsorbed CO_2 becomes active in IR as a consequence of the dipole perpendicular to the surface, which increases once the molecule bends. In addition, the bending of the molecule upon

adsorption leads to an increase in the value of the bending mode (δ) with an average calculated shift of 79 cm^{-1}.

3.3. Electronic Structure. In Table 1, we have included the Bader charge analysis of the Ni$_n$ clusters before and after CO$_2$ adsorption. The average calculated charge for Ni$_n$ clusters supported on YSZ(111) is +0.2 e$^-$ (i.e., loss of 0.2 e$^-$). However, the charge distribution within the cluster is not uniform: the Ni atoms located at the interface with the surface are positively charged (an average of +0.1 e$^-$), whereas the Ni atoms at the top are negatively charged (an average of −0.1 e$^-$). Once CO$_2$ adsorbs, the Ni atoms interacting with CO$_2$ lose an average of 0.3 electrons: the top Ni atom (Ni^2—Figure 3) oxidizes from −0.1 e$^-$ to +0.2 e$^-$, whereas the charge of the bottom Ni atom (Ni^1—Figure 3), directly interacting with CO$_2$, increases from +0.1 e$^-$ to +0.4 e$^-$.

As to the CO$_2$ molecule, we have evaluated an average charge gain of 0.8 e$^-$ upon adsorption on the Ni$_n$-YSZ(111) (n = 4−7, 10, and 20) interface, which comes mainly from the Ni$_n$ clusters because the charge of the surface atoms neighboring CO$_2$ remains unchanged.

We have characterized the adsorbed CO$_2$ species by plotting the electron density difference as $\Delta\rho = \rho_{(CO_2-surface)} - (\rho_{(surface)} + \rho_{(CO_2)})$ in Figure 6, which shows charge accumulation
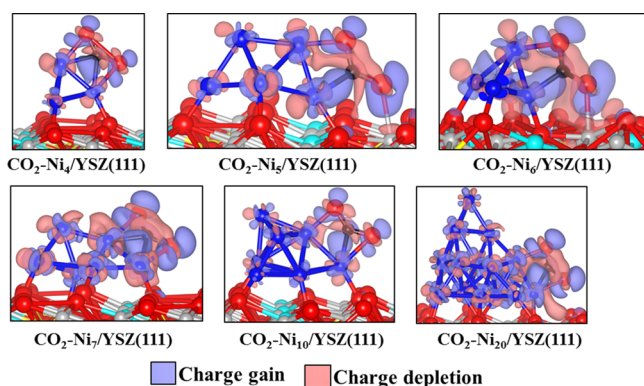

Figure 6. Calculated electron density differences for the most favorable CO$_2$ adsorption on the Ni$_n$ (n = 4−7, 10, and 20)-decorated YSZ(111) surfaces. Color key: O, Zr, Y, Ni, and C are represented by red, gray, cyan, blue, and black spheres, respectively. The yellow spheres represent the oxygen vacancy.

between the CO$_2$ oxygens and the cluster. The strong CO$_2$−Ni$_n$/YSZ(111) (n = 4−7, 10, and 20) interactions come mainly from C−Ni$_n$ bond formation, as shown by the accumulation of charge density between the C and the metal cluster. We have observed a polarization of the CO$_2$ oxygen atom by the surface oxygen and zirconium in CO$_2$−Ni$_n$/YSZ(111) (n = 5 and 6), since there is a depletion of charge between the CO$_2$ oxygen and the surface atoms. This finding is in good agreement with the charge transfer from the surface atom to the molecule discussed previously. The electron density difference analysis confirms our previous observation, i.e., that the CO$_2$−Ni$_n$/YSZ(111) (n = 4−7, 10, and 20) interaction is mainly due to the interaction of the CO$_2$ molecule with the Ni$_n$ cluster.

The representation of the projected DOS of CO$_2$−Ni$_n$/YSZ(111) (n = 4−7, 10, and 20) (Figure 7) reveals peaks in the band gap of the YSZ surface corresponding to d-type Ni orbitals. The number of the d-type orbitals in the band gap increases with the cluster size, as it has also been shown previously on the Ni$_n$/CeO$_2$ surface.[35] There is metal d mixing
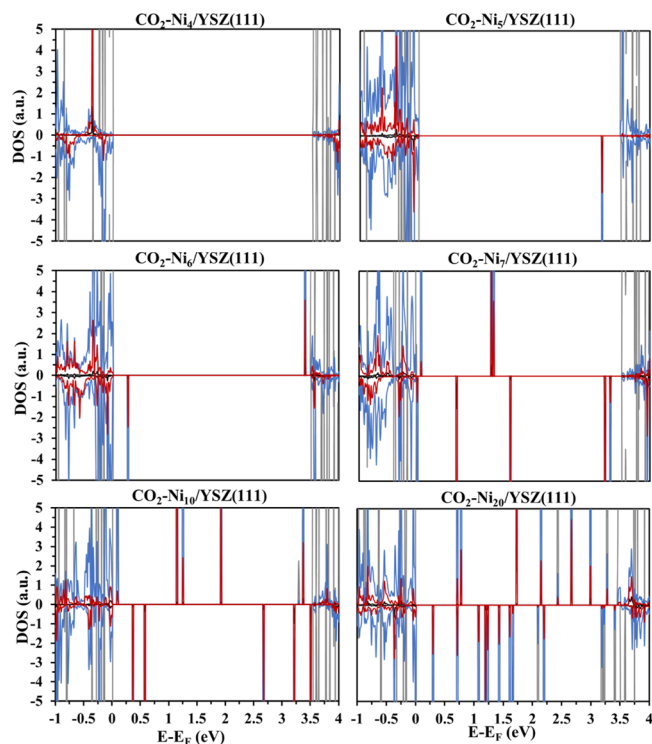

Figure 7. Total density of states (DOS) of CO$_2$−Ni$_n$/YSZ(111) in gray and projected DOS on C of CO$_2$, O of CO$_2$, and Ni$_n$ clusters in black, red, and blue, respectively.

with the CO$_2$ orbitals, leading to bonding and antibonding states related to the bending of the molecule upon adsorption. This behavior is similar to that found by Choe et al.,[75] in their investigation of the adsorption of CO$_2$ on Pt(111) and Fe(111). They used the atom superposition and delocalization molecular orbital theory to show the relation of the bending of CO$_2$ on the surfaces with the mixing of the d metal orbitals and the CO$_2$ orbitals. They have calculated the binding energies of 3.73 and 1.70 eV on Fe(111) and Pt(111) surfaces, respectively. Thus, CO$_2$ adsorption is stronger on these metallic surfaces than on the Ni/YSZ(111) surface, as the largest binding energy calculated here is 1.66 eV for the Ni$_6$/YSZ(111) surface.

3.4. Reverse WGSR. We have studied the catalytic properties of the Ni$_n$/YSZ interface for the reverse water gas shift (RWGS) reaction (eq 2) by proposing one of the possible reaction paths

$$CO_2 + H_2 \leftrightarrow CO + H_2O \qquad (2)$$

We have chosen to study the RWGS reaction for a relatively small cluster size, i.e., Ni$_5$/YSZ(111), based on the above findings that the CO$_2$ adsorption geometry is similar regardless of the Ni cluster size. The adsorbate binds at the edge of the cluster with a minimal interaction with the YSZ surface.

We have tried several adsorption sites and orientations of the H$_2$ molecule and show the most stable geometry of H$_2$−Ni$_5$/YSZ(111) in Figure 8.

From Figure 8, we see that H$_2$ adsorbs dissociatively on Ni$_5$/YSZ(111), and each hydrogen sits on a facet of the triangular pyramid Ni cluster. The homolytic dissociation of H$_2$ upon adsorption on Ni$_5$/YSZ observed in this investigation is in good agreement with previous studies.[63,76−78] The calculated binding energy is −1.51 eV, and we note a charge transfer from
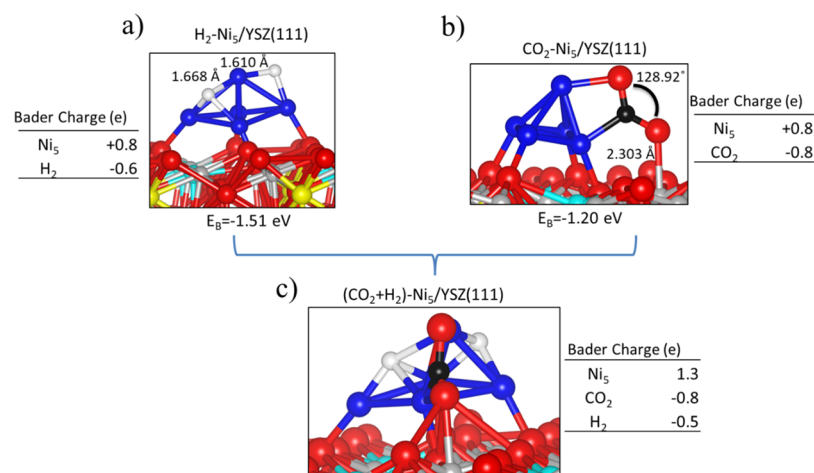
Figure 8. Representation of the most stable configurations of (a) H_2, (b) CO_2, and (c) CO_2-H_2 on Ni_5/YSZ(111). The Bader charges of the adsorbed molecules are shown next to each configuration. Color key: O, Zr, Y, Ni, C, and H are represented by red, gray, cyan, blue, black, and white spheres, respectively. The yellow spheres represent the oxygen vacancy.
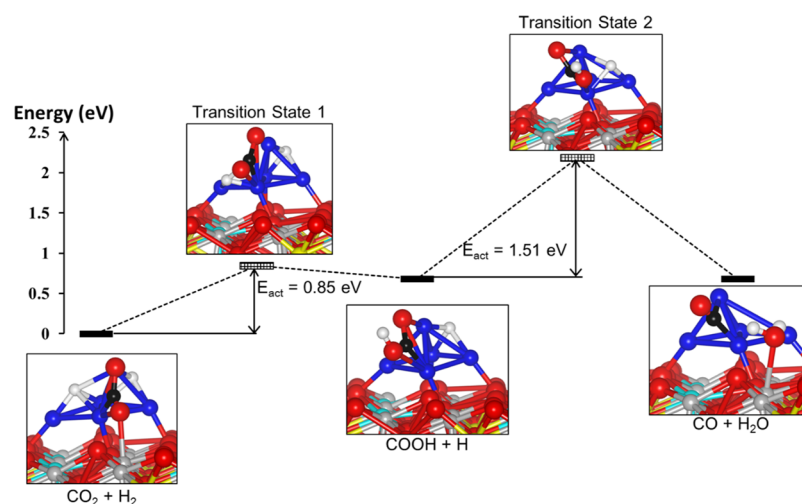

Figure 9. Energy profile showing reactants, intermediates, transition states, and final products for the RWGS reaction on the Ni_5/YSZ(111) interface. E_{act} corresponds to the activation energy between the initial and final states and the intermediate state. The energy of the reactants is set to zero. Color key: O, Zr, Y, Ni, C, and H are represented by red, gray, cyan, blue, black, and white spheres, respectively. The yellow spheres represent the oxygen vacancy.

the Ni_5/YSZ(111) to both hydrogen atoms (Figure 8 a). H_2 and CO_2 adsorb on Ni_5/YSZ(111) with a similar binding energy (Figure 8). However, we did not find competition of the adsorbates for the same adsorption sites. This led us to consider a geometry where hydrogen atoms are adsorbed on the faces of the metal cluster and the CO_2 molecule on its edge. Figure 8c corresponds to the most stable geometry of the $(CO_2-H_2)-Ni_5$/YSZ(111) system, which is the starting point of the RWGS reaction (eq 2).

During the RWGS reaction, one of the H atoms can either go toward the CO_2 oxygen or carbon atom. In the first alternative, the reaction proceeds through a hydrocarboxylic intermediate (COOH), whereas in the second case, the intermediate is a formate (HCOO). We have investigated the hydrocarboxylic pathway of the RWGS reaction by identifying the structures and calculating the energies of the intermediate state and two transition states (Figure 9), which had been identified using the dimer method.[79]

Figure 9 shows the first step of the RWGS reaction pathway, where a hydrogen atom migrates toward its nearest CO_2

oxygen to form the hydrocarboxylic intermediate (COOH). The energy difference between the first transition state and the initial state $((CO_2 + H_2)-Ni_5$/YSZ(111)), i.e., the activation energy, is equal to 0.85 eV. The second step involves the protonation of the hydrogenated CO_2 oxygen, allowing the formation of H_2O (adsorbed on the surface) and the CO molecule (adsorbed on the Ni cluster). This step goes through a transition state with an activation energy of 1.51 eV, which is higher than the previous barrier (0.85 eV) and the latter is thus the rate-limiting step of the overall pathway. This large activation energy (1.51 eV) explains the high temperature needed (above 810 °C) to achieve the RWGS reaction. Previous theoretical investigations of CO_2 hydrogenation on similar metal−oxides interfaces have also determined high barriers to form the transition states in their reaction pathways.[36−38]

4. CONCLUSIONS

We have used DFT+D calculations to investigate the interaction of CO_2 with the clean YSZ(111) surface and

with the interface of YSZ(111) and supported Ni_n (n = 1, 4−7, 10, and 20) particles. The molecule adsorbs weakly on the clean YSZ(111) surface and at a single supported Ni atom. However, it bends and activates at the interfaces between the Ni_n (n = 4−7, 10, and 20) particles and the YSZ surface. The C−O distance, as well as the vibrational stretching and bending modes, confirms the activation of the molecule along the bending mode and a shift of the asymmetrical stretching mode. The Bader charge analysis demonstrates a charge transfer from the Ni_n cluster to the molecule, with the electron density difference plot, indicating a charge accumulation between the Ni atoms and the CO_2 molecule, which is further evidenced by the mixing of the metal d orbitals with the CO_2 molecule, as described in the DOS analysis. These observations led us to conclude that the CO_2 interaction with the Ni_n/YSZ(111) (n = 4−7, 10, and 20) interfaces is similar and independent of the Ni particle size beyond a minimum size. Next, we have studied the hydrocarboxylic pathway for the RWGS reaction including the thermodynamic and kinetic analysis of the energy profile. Our calculations showed that the second transition state, from COOH intermediate to CO and H_2O products, is the rate-limiting step of the overall reaction with a barrier energy of 1.51 eV.

■ AUTHOR INFORMATION

Corresponding Author
*E-mail: DeLeeuwN@cardiff.ac.uk. Phone: +44 (0) 2920870658.

ORCID ●
Abdelaziz Cadi-Essadek: 0000-0002-7754-735X
Nora H. de Leeuw: 0000-0002-8271-0545

Notes
The authors declare no competing financial interest.

■ ACKNOWLEDGMENTS

■ REFERENCES

(1) Pan, Y.-x.; Liu, C.-j.; Wiltowski, T. S.; Ge, Q. CO_2 adsorption and activation over γ-Al_2O_3-supported transition metal dimers: A density functional study. *Catal. Today* **2009**, *147*, 68−76.

(2) Jensen, S. H.; Larsen, P. H.; Mogensen, M. Hydrogen and synthetic fuel production from renewable energy sources. *Int. J. Hydrogen Energy* **2007**, *32*, 3253−3257.

(3) Ebbesen, S. D.; Mogensen, M. Electrolysis of carbon dioxide in Solid Oxide Electrolysis Cells. *J. Power Sources* **2009**, *193*, 349−358.

(4) Graves, C.; Ebbesen, S. D.; Mogensen, M. Co-electrolysis of CO_2 and H_2O in solid oxide cells: Performance and durability. *Solid State Ionics* **2011**, *192*, 398−403.

(5) Hartvigsen, J.; et al.. Carbon Dioxide Recycling By High Temperature Co-Electrolysis And Hydrocarbon Synthesis. *ECS Transaction*, 2008, Vol. 12, pp 171−182.

(6) Yang, C.; et al. Co-electrolysis of H_2O and CO_2 in a solid oxide electrolysis cell with hierarchically structured porous electrodes. *J. Mater. Chem. A* **2015**, *3*, 15913−15919.

(7) Zhan, Z.; et al. Syngas Production By Coelectrolysis of CO_2/H_2O: The Basis for a Renewable Energy Cycle. *Energy Fuels* **2009**, *23*, 3089−3096.

(8) Fu, Q.; Mabilat, C.; Zahid, M.; Brisse, A.; Gautier, L. Syngas production via high-temperature steam/CO_2 co-electrolysis: an economic assessment. *Energy Environ. Sci.* **2010**, *3*, 1382−1397.

(9) Hauch, A.; Ebbesen, S. D.; Jensen, S. H.; Mogensen, M. Highly efficient high temperature electrolysis. *J. Mater. Chem.* **2008**, *18*, 2331.

(10) Minh, N. Q. Ceramic Fuel Cells. *J. Am. Ceram. Soc.* **1993**, *76*, 563−588.

(11) Singhal, S. C. Science and Technology of Solid-Oxide Fuel Cells. *MRS Bull.* **2000**, *25*, 16−21.

(12) Yamamoto, O. Solid oxide fuel cells: fundamental aspects and prospects. *Electrochim. Acta* **2000**, *45*, 2423−2435.

(13) Steele, B. C. H. Material science and engineering: The enabling technology for the commercialisation of fuel cell systems. *J. Mater. Sci.* **2001**, *36*, 1053−1068.

(14) Huijsmans, J. Ceramics in solid oxide fuel cells. *Curr. Opin. Solid State Mater. Sci.* **2001**, *5*, 317−323.

(15) Gorte, R. J. Recent developments towards commercialization of solid oxide fuel cells. *AIChE J.* **2005**, *51*, 2377−2381.

(16) de Bruijn, F. The current status of fuel cell technology for mobile and stationary applications. *Green Chem.* **2005**, *7*, 132−150.

(17) Kendall, K. Progress in solid oxide fuel cell materials. *Int. Mater. Rev.* **2005**, *50*, 257−264.

(18) Sun, C.; Stimming, U. Recent anode advances in solid oxide fuel cells. *J. Power Sources* **2007**, *171*, 247−260.

(19) Ormerod, R. M. Solid oxide fuel cells. *Chem. Soc. Rev.* **2003**, *32*, 17−28.

(20) Park, S.; Vohs, J. M.; Gorte, R. J. Direct oxidation of hydrocarbons in a solid-oxide fuel cell. *Nature* **2000**, *404*, 265−267.

(21) Steele, B. C. H.; Heinzel, A. Materials for fuel-cell technologies. *Nature* **2001**, *414*, 345−352.

(22) Koide, H.; Someya, Y.; Yoshida, T.; Maruyama, T. Properties of Ni/YSZ cermet as anode for SOFC. *Solid State Ionics* **2000**, *132*, 253−260.

(23) Ribeiro, N. F. P.; Souza, M. M. V. M.; Neto, O. R. M.; Vasconcelos, S. M. R.; Schmal, M. Investigating the microstructure and catalytic properties of Ni/YSZ cermets as anodes for SOFC applications. *Appl. Catal., A* **2009**, *353*, 305−309.

(24) Qiao, J.; et al. Ni/YSZ and Ni-CeO_2/YSZ anodes prepared by impregnation for solid oxide fuel cells. *J. Power Sources* **2007**, *169*, 253−258.

(25) Muñoz, M. C.; Gallego, S.; Beltrán, J. I.; Cerdá, J. Adhesion at metal-ZrO_2 interfaces. *Surf. Sci. Rep.* **2006**, *61*, 303−344.

(26) Bogicevic, A.; Wolverton, C.; Crosbie, G. M.; Stechel, E. B. Defect ordering in aliovalently doped cubic zirconia from first principles. *Phys. Rev. B: Condens. Matter Mater. Phys.* **2001**, *64*, 14106.

(27) Aldebert, P.; Traverse, J.-P. Structure and Ionic Mobility of Zirconia at High Temperature. *J. Am. Ceram. Soc.* **1983**, *68*, 34−40.

(28) Ebrahim, R.; Yeleuov, M.; Issova, A.; Tokmoldin, S.; Ignatiev, A. Triple-phase boundary and power density enhancement in thin solid oxide fuel cells by controlled etching of the nickel anode. *Nanoscale Res. Lett.* **2014**, *9*, 286.

(29) Chen, X.; Wu, N. J.; Smith, L.; Ignatiev, A. Thin-film heterostructure solid oxide fuel cells. *Appl. Phys. Lett.* **2004**, *84*, 2700−2702.

(30) Zhu, W. Z.; Deevi, S. C. A review on the status of anode materials for solid oxide fuel cells. *Mater. Sci. Eng., A* **2003**, *362*, 228−239.

(31) Novosel, B.; Avsec, M.; Macek, J. The Interaction of SOFC Anode Materials With Carbon Monoxide. *Mater. Technol.* **2008**, *42*, 51−57.

(32) Matsuzaki, Y.; Yasuda, I. Electrochemical Oxidation of H_2 and CO in a H_2-H_2O-CO-CO_2 System at the Interface of a Ni-YSZ Cermet Electrode and YSZ Electrolyte. *J. Electrochem. Soc.* **2000**, *147*, 1630−1635.

(33) Andreassi, L.; Toro, C.; Ubertini, S. Modeling Carbon Monoxide Direct Oxidation in Solid Oxide Fuel Cells. *J. Fuel Cell Sci. Technol.* **2009**, *6*, 021307.

(34) Hahn, K. R.; Iannuzzi, M.; Seitsonen, A. P.; Hutter, J. Coverage Effect of the CO_2 Adsorption Mechanisms on CeO_2(111) by First Principles Analysis. *J. Phys. Chem. C* **2013**, *117*, 1701−1711.

(35) Hahn, K. R.; Seitsonen, A. P.; Iannuzzi, M.; Hutter, J. Functionalization of CeO_2(111) by Deposition of Small Ni Clusters: Effects on CO_2 Adsorption and O Vacancy Formation. *ChemCatChem* **2015**, *7*, 625−634.

(36) Liu, C.; et al. Carbon Dioxide Conversion to Methanol over Size-Selected Cu_4 Clusters at Low Pressures. *J. Am. Chem. Soc.* **2015**, *137*, 8676−8679.

(37) Zhang, R.; Wang, B.; Liu, H.; Ling, L. Effect of Surface Hydroxyls on CO_2 Hydrogenation Over Cu/γ-Al_2O_3 Catalyst: A Theoretical Study. *J. Phys. Chem. C* **2011**, *115*, 19811−19818.

(38) Pan, Y.-x.; Liu, C.-j.; Ge, Q. Effect of surface hydroxyls on selective CO_2 hydrogenation over Ni_4/γ-Al_2O_3: A density functional theory study. *J. Catal.* **2010**, *272*, 227−234.

(39) Yang, Y.; Evans, J.; Rodriguez, J. A.; White, M. G.; Liu, P. Fundamental studies of methanol synthesis from CO_2 hydrogenation on Cu(111), Cu clusters, and Cu/ZnO(000$\bar{1}$). *Phys. Chem. Chem. Phys.* **2010**, *12*, 9909−9917.

(40) Vidal, A. B.; et al. CO_2 Activation and Methanol Synthesis on Novel Au/TiC and Cu/TiC Catalysts. *J. Phys. Chem. Lett.* **2012**, *3*, 2275−2280.

(41) Yin, S.; Swift, T.; Ge, Q. Adsorption and activation of CO_2 over the Cu-Co catalyst supported on partially hydroxylated γ-Al_2O_3. *Catal. Today* **2011**, *165*, 10−18.

(42) Tang, Q.-L.; Hong, Q.-J.; Liu, Z.-P. CO_2 fixation into methanol at Cu/ZrO_2 interface from first principles kinetic Monte Carlo. *J. Catal.* **2009**, *263*, 114−122.

(43) Grau-Crespo, R.; Hernández, N. C.; Sanz, J. F.; de Leeuw, N. H. Theoretical Investigation of the Deposition of Cu, Ag, and Au Atoms on the ZrO_2(111) Surface. *J. Phys. Chem. C* **2007**, *111*, 10448−10454.

(44) Cadi-Essadek, A.; Roldan, A.; de Leeuw, N. H. Ni Deposition on Yttria-Stabilized ZrO_2(111) Surfaces: A Density Functional Theory Study. *J. Phys. Chem. C* **2015**, *119*, 6581−6591.

(45) Watson, G. W.; Kelsey, E. T.; de Leeuw, N. H.; Harris, D. J.; Parker, S. C. Atomistic simulation of dislocations, surfaces and interfaces in MgO. *J. Chem. Soc., Faraday Trans.* **1996**, *92*, 433.

(46) Pietrucci, F.; Bernasconi, M.; Laio, A.; Parrinello, M. Vacancy-vacancy interaction and oxygen diffusion in stabilized cubic ZrO_2 from first principles. *Phys. Rev. B: Condens. Matter Mater. Phys.* **2008**, *78*, 94301.

(47) Xia, X.; Oldman, R.; Catlow, R. Computational Modeling Study of Bulk and Surface of Yttria-Stabilized Cubic Zirconia. *Chem. Mater.* **2009**, *21*, 3576−3585.

(48) Cadi-Essadek, A.; Roldan, A.; de Leeuw, N. H. Stability and Mobility of Supported Ni_n (n = 1−10) Clusters on ZrO_2(111) and YSZ(111) Surfaces: a Density Functional Theory Study. *Faraday Discuss.* **2017**, DOI: 10.1039/c7fd00217c.

(49) Tosoni, S.; Chen, H.-Y. T.; Pacchioni, G. A DFT study of Ni clusters deposition on titania and zirconia (101) surfaces. *Surf. Sci.* **2016**, *646*, 230−238.

(50) Hohenberg, P.; Kohn, W. Inhomogeneous electron gas. *Phys. Rev.* **1964**, *136*, B864−B871.

(51) Kresse, G.; Furthmüller, J. Efficient iterative schemes for ab initio total-energy calculations using a plane-wave basis set. *Phys. Rev. B: Condens. Matter Mater. Phys.* **1996**, *54*, 11169−11186.

(52) Kresse, G.; Furthmüller, J. Efficiency of ab-initio total energy calculations for metals and semiconductors using a plane-wave basis set. *Comput. Mater. Sci.* **1996**, *6*, 15−50.

(53) Kresse, G.; Hafner, J. Ab initio molecular dynamics for open-shell transition metals. *Phys. Rev. B: Condens. Matter Mater. Phys.* **1993**, *48*, 13115−13118.

(54) Kresse, G.; Hafner, J. Norm-conserving and ultrasoft pseudopotentials for first-row and transition elements. *J. Phys.: Condens. Matter* **1994**, *6*, 8245−8257.

(55) Perdew, J. P.; Burke, K.; Ernzerhof, M. Generalized gradient approximation made simple. *Phys. Rev. Lett.* **1996**, *77*, 3865−3868.

(56) Grimme, S. Semiempirical GGA-type density functional constructed with a long-range dispersion correction. *J. Comput. Chem.* **2006**, *27*, 1787−1799.

(57) Dzade, N. Y.; Roldan, A.; De Leeuw, N. H. Activation and dissociation of CO_2 on the (001), (011), and (111) surfaces of mackinawite (FeS): A dispersion-corrected DFT study. *J. Chem. Phys.* **2015**, *143*, 094703.

(58) Tafreshi, S. S.; Roldan, A.; de Leeuw, N. H. Hydrazine network on Cu(111) surface: A Density Functional Theory approach. *Surf. Sci.* **2015**, *637*−*638*, 140−148.

(59) Haider, S.; Roldan, A.; de Leeuw, N. H. Catalytic Dissociation of Water on the (001), (011), and (111) Surfaces of Violarite, $FeNi_2S_4$: A DFT-D2 Study. *J. Phys. Chem. C* **2014**, *118*, 1958−1967.

(60) Blöchl, P. E. Projector augmented-wave method. *Phys. Rev. B: Condens. Matter Mater. Phys.* **1994**, *50*, 17953−17979.

(61) Zhang, Y.; Fu, Z.; Dong, S.; Yang, Z. The mechanisms for the high resistance to sulfur poisoning of the Ni/yttria-stabilized zirconia system treated with Sn vapor. *Phys. Chem. Chem. Phys.* **2014**, *16*, 1033−1040.

(62) Shishkin, M.; Ziegler, T. The Oxidation of H_2 and CH_4 on an Oxygen-Enriched Yttria-Stabilized Zirconia Surface: A Theoretical Study Based on Density Functional Theory. *J. Phys. Chem. C* **2008**, *112*, 19662−19669.

(63) Shishkin, M.; Ziegler, T. Hydrogen Oxidation at the Ni/Yttria-Stabilized Zirconia Interface: A Study Based on Density Functional Theory. *J. Phys. Chem. C* **2010**, *114*, 11209−11214.

(64) French, R. H.; Glass, S. J.; Ohuchi, F. S.; Xu, Y.-N.; Ching, W. Y. Experimental and theoretical determination of the electronic structure and optical properties of three phases of ZrO_2. *Phys. Rev. B: Condens. Matter Mater. Phys.* **1994**, *49*, 5133−5142.

(65) Sayan, S.; et al. Valence and conduction band offsets of a ZrO_2/SiO_xN_y/n-Si CMOS gate stack: A combined photoemission and inverse photoemission study. *Phys. Status Solidi B* **2004**, *241*, 2246−2252.

(66) Alfredsson, M.; Catlow, C. R. A. Modelling of Pd and Pt supported on the {111} and {011} surfaces of cubic-ZrO_2. *Phys. Chem. Chem. Phys.* **2001**, *3*, 4129−4140.

(67) Bader, R. F. W. A quantum theory of molecular structure and its applications. *Chem. Rev.* **1991**, *91*, 893−928.

(68) Cadi-Essadek, A.; Roldan, A.; de Leeuw, N. H. Density functional theory study of the interaction of H_2O, CO_2 and CO with the ZrO_2(111), Ni/ZrO_2(111), YSZ(111) and Ni/YSZ(111) surfaces. *Surf. Sci.* **2016**, *653*, 153−162.

(69) Chen, H.-Y. T.; Tosoni, S.; Pacchioni, G. A DFT study of the acid-base properties of anatase TiO_2 and tetragonal ZrO_2 by adsorption of CO and CO_2 probe molecules. *Surf. Sci.* **2016**, *652*, 163−171.

(70) Shimanouchi, J. "Molecular Vibrational Frequencies" in NIST Chemistry WebBook. *NIST Standard Reference Database Number 69*; Linstrom, P. J., Mallard, W. G., Eds.; National Institute of Standards and Technology: Gaithersburg MD, 20899, http://webbook.nist.gov. http://webbook.nist.gov, (accessed August 2015).

(71) Ramis, G.; Busca, G.; Lorenzelli, V. Low-temperature CO_2 adsorption on metal oxides: spectroscopic characterization of some weakly adsorbed species. *Mater. Chem. Phys.* **1991**, *29*, 425−435.

(72) Mudiyanselage, K.; et al. Importance of the Metal-Oxide Interface in Catalysis: In Situ Studies of the Water-Gas Shift Reaction by Ambient-Pressure X-ray Photoelectron Spectroscopy. *Angew. Chem., Int. Ed.* **2013**, *52*, 5101−5105.

(73) Graciani, J.; Mudiyanselage, K.; Xu, F.; Baber, A. E.; Evans, J.; Senanayake, S. D.; Stacchiola, D. J.; Liu, P.; Hrbek, J.; Sanz, J. F.; Rodriguez, J. A. Highly active copper-ceria and copper-ceria-titania catalysts for methanol synthesis from CO_2. *Science* **2014**, *345*, 546−550.

(74) Seiferth, O.; et al. IR investigations of CO_2 adsorption on chromia surfaces: Cr_2O_3 (0001)/Cr(110) versus polycrystalline α-Cr_2O_3. *Surf. Sci.* **1999**, *421*, 176−190.

(75) Choe, S. J.; Park, D. H.; Huh, D. S. Adsorption and Dissociation Reaction of Carbon Dioxide on Pt(111) and Fe(111) Surface: MO-study. *Bull. Korean Chem. Soc.* **2000**, *21*, 779−784.

(76) Cucinotta, C. S.; Bernasconi, M.; Parrinello, M. Hydrogen Oxidation Reaction at the Ni/YSZ Anode of Solid Oxide Fuel Cells from First Principles. *Phys. Rev. Lett.* **2011**, *107*, 206103.

(77) Ammal, S. C.; Heyden, A. Combined DFT and Microkinetic Modeling Study of Hydrogen Oxidation at the Ni/YSZ Anode of Solid Oxide Fuel Cells. *J. Phys. Chem. Lett.* **2012**, *3*, 2767−2772.

(78) Iskandarov, A. M.; Tada, T. Dopant driven tuning of the hydrogen oxidation mechanism at the pore/nickel/zirconia triple phase boundary. *Phys. Chem. Chem. Phys.* **2018**, *20*, 12574−12588.

(79) Heyden, A.; Bell, A. T.; Keil, F. J. Efficient methods for finding transition states in chemical reactions: comparison of improved dimer method and partitioned rational function optimization method. *J. Chem. Phys.* **2005**, *123*, 224101.